Chapter 3

A Reconfigurable On-Board Power Converter for Electric Vehicles

3.1 Introduction

The conventional powertrain architecture of a standard electric vehicle (EV) is shown in Fig. 3.1. This contains two major power-processing units; one that draws power from the EV battery pack and supply power to the driving motor that makes the vehicle move and the other unit draws power from the AC supply and charges the battery pack. It may be observed from Fig. 3.1 that for battery charging, typically two power stages are used, namely: 1) boost rectifier power factor correction (PFC) stage for near-unity power factor operation on input side and 2) step-down DC-DC conversion stage to step-down the front-end converter output voltage to a level suitable for charging the battery. Further, it is also clear from Fig. 3.1 that a voltage source inverter (VSI) is needed to drive the motor of EV. Thus, it can be inferred that a conventional EV requires two separate power-processing units for motoring and charging as shown in Fig. 3.1.

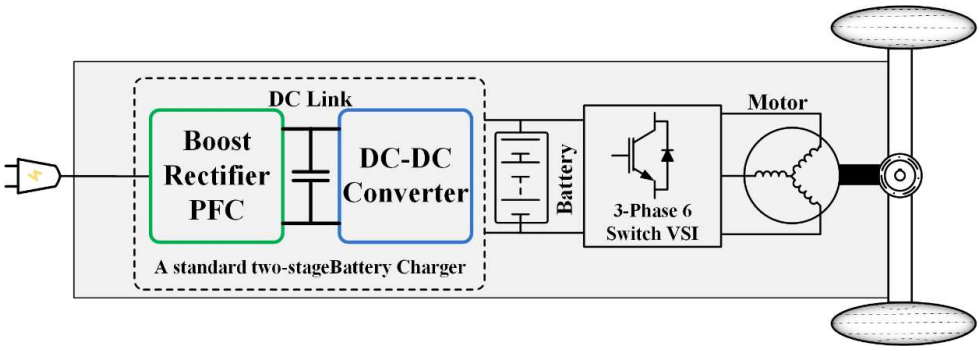

Fig. 3.1. Conventional charger topology for charging low voltage battery packs.

To minimize the number of power processing units, recent research proposes to integrate the on-board charger with the motor drive unit. This integrated single unit that charges the EV battery pack and drive the motor unit is termed as integrated charger. Most of the integrated chargers reutilize the components from motoring (propulsion) operation and make use of it during charging operation. In an EV, propulsion and charging operations are two

mutually exclusive operations as discussed in chapter 1. From the literature survey, it is clear that the already reported topologies either use motor windings as inductors (boost inductors or filter inductors) or they require an additional power stage for rectification or they do not have galvanic isolation between AC supply and the battery pack.

In order to optimize the number of elements in the integrated power-processing unit and to reduce the cost, volume and weight of the EV, a single converter topology is proposed in this work. The proposed converter can be reconfigured into a three -phase VSI during propulsion mode and an EV battery charger during charging mode. The details of reconfiguration process, design and mathematical analysis in both the modes are explained in this chapter with experimental verification. In propulsion mode, the converter transfers power from the battery to the traction motor. During charging mode, the same converter is reconfigured to obtain a two-stage battery charger. The first stage of the reconfigured battery charger is a boost rectifier power factor corrector and the second stage is a DC-DC converter. Both the stages are cascaded by a common DC-link. Thus, in the proposed topology, the three-leg structure (six MOSFETs) is reconfigured as a charger for optimal charging of the EV battery pack during charging mode and as an inverter to drive the electric traction motor during the propulsion mode. This enables the integration of the charger with the drive unit of the EV, which leads to reduction in weight, volume and cost of the overall system. The proposed power converter reutilizes all the MOSFETs during both the propulsion and charging modes, unlike the reported topologies that use only some of the components of motoring mode to form the charging mode.

The schematic of the proposed topology is shown in Fig. 3.2. The two boxes indicating the modes of operation of the converter represents the reconfigurable nature of the topology. Hence, the two boxes indicating two different converters are effectively amalgamated into one reconfigurable converter represented by the red box. The battery and the motor along with the axle (as present in a traditional EV) are illustrated in Fig. 3.2.

A three-phase VSI is the backbone of the proposed converter that can either be reconfigured as a propulsion unit or a battery charger unit by adding few more power electronic components. During charging mode, the proposed topology is reconfigured to form a front-end boost converter with PFC and a DC-DC converter (with galvanic isolation), both sharing a common DC-link. The same power stage is reconfigured to operate as a three-phase VSI to

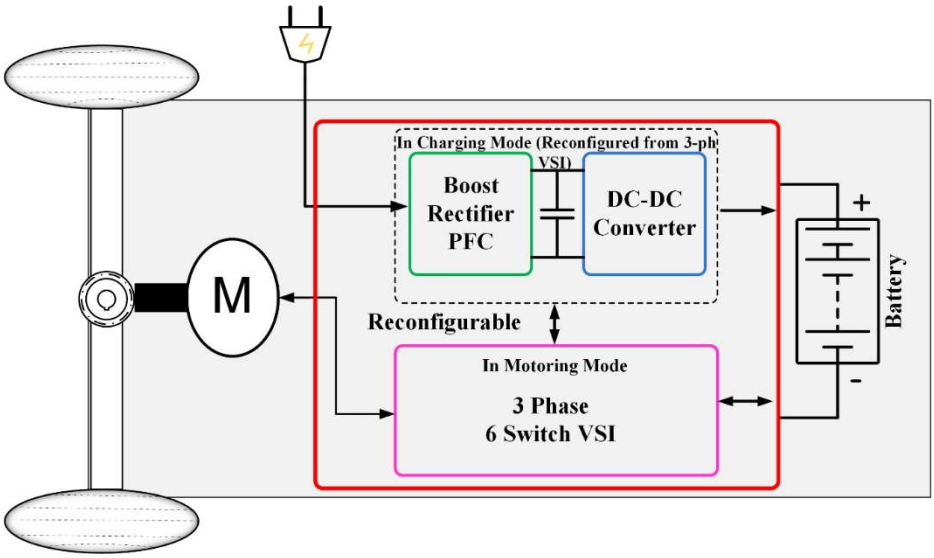

Fig. 3.2. Proposed reconfigurable integrated battery charger.

drive the traction motor during the propulsion mode. Thus, it reduces the switch count by eliminating the requirement of a separate inverter stage. Simultaneously; the weight, volume and cost of the overall system also reduce. A 500 W scaled-down prototype is developed and its performance is validated with constant current-constant voltage (CC-CV) charging of a 24 V, 30Ah battery pack in charging mode and with a 400W brushless DC (BLDC) motor in propulsion mode.

In a conventional EV, the on-board charger requires multiple control loops to control multiple stages of the charger. For example, a two-stage on-board EV charger requires two different control loops for each stage (AC-DC boost rectifier and DC-DC isolated converter). To reduce the control complexity, a novel control architecture termed as "unified control loop" is proposed in this work, which is capable to achieve near unity power factor operation of front-end boost rectifier and optimal battery charging without sensing the DC-link voltage. Hence, the need for separate control loops for each of the power stages is eliminated in the proposed topology. Further, the sensor used at the DC-link terminal is saved as there is no need to sense the DC-link voltage in the proposed control scheme. This eases the design process and also saves computational requirements.

3.2 Derivation of the Topology

The motivation behind the reconfiguring the proposed topology is to integrate a battery charger into the drive unit of an EV in such a way that the charger obtained is a two-stage converter with a boost rectifier input PFC stage followed by a DC-DC converter with a common DC-link. Since a three-phase, 6-switchVSI is widely used for driving traction motors, it could be considered as the starting point in deriving the EV charger. A three- phase VSI has three half-bridge switch legs; hence, in the charging mode, these legs have to be reassigned for

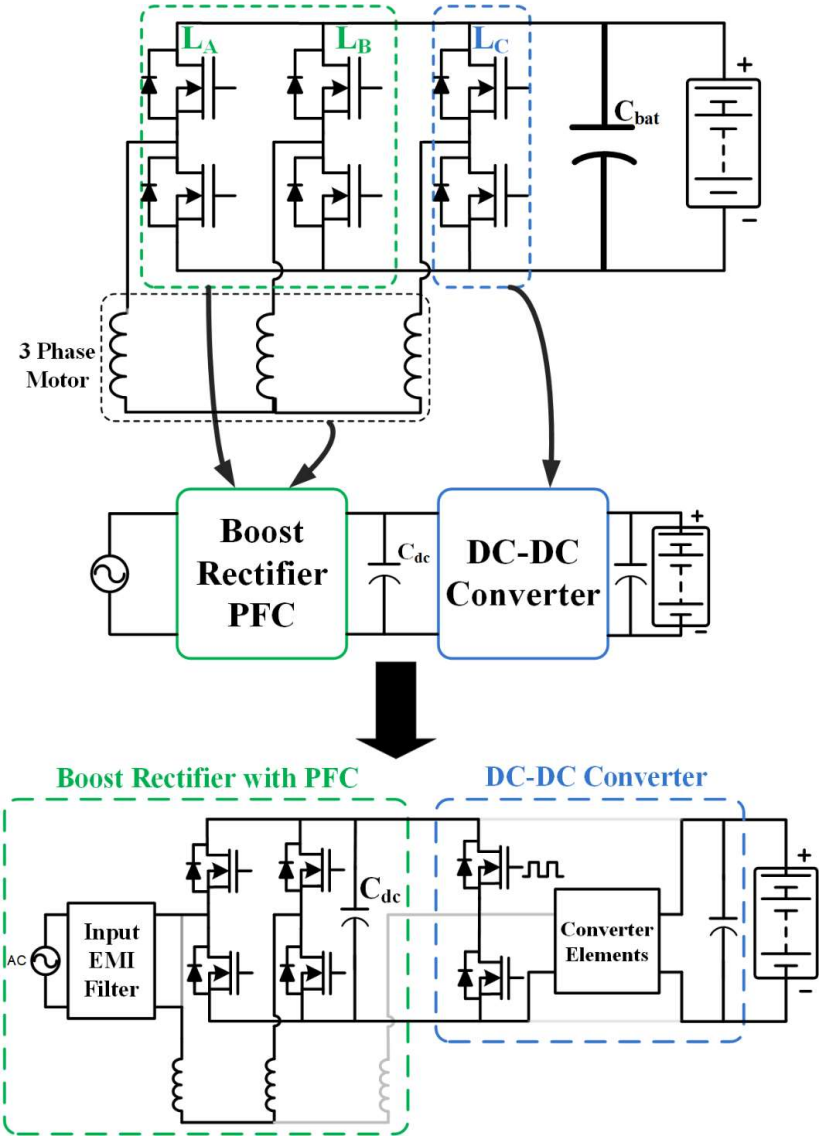

Fig. 3.3. Derivation of the integrated battery charger from a three -phase VSI fed traction motor.

AC-DC boost rectifier and DC-DC isolated converter. Fig. 3.3 shows the process of deriving the integrated battery charger from a three -phase VSI fed traction motor. The three -phase VSI legs L_A and L_B are operated as asymmetrical two-device unidirectional boost converter. The remaining leg L_C is used to construct a half-bridge LLC converter for the DC-DC stage.

Two of the motor phase windings connected in series (as shown in Fig. 3.3) act as the boost inductor at the input side of the AC-DC rectifier stage. Only motor phase windings PH_1 and PH_2 are used during the charging mode, while the motor phase winding PH_3 remains idle. Usually, the charging time period is significantly less as compared to its corresponding motoring duration, and hence its effect in the life time of the motor is very less. However, litz wires can be used for designing windings of the motor to further increase the life time of the motor.

The DC-DC converter includes a centre-tapped transformer with leakage inductance L_r and magnetizing inductance L_m, a resonant capacitor C_r and diodes D_1, D_2. The inductance values of L_r and L_m can be utilized as resonant components of the LLC resonant network [120]. A DC-link capacitor is used between the two converter stages to maintain the DC-link voltage constant.

The motor windings are re-utilized as the boost inductance in the charging mode. The voltage rating of the motor is proportional to the back EMF generated, which is generally proportional to the number of stator winding turns of the motor. The number of winding turns determines the winding inductance. This implies that the winding inductance of low voltage motors can be low. The low input inductance results into considerable input current ripple. The addition of an external inductance on the input side in series with the motor phase windings may be required to mitigate the high current ripple.

The proposed reconfigurable on-board power converter (R-OPC) topology is reconfigured into a two-stage single-phase battery charger from a three -phase VSI and vice versa. Thus, a switching mechanism is needed for transition from one mode to another. Five electromechanical contactors (Form-1C) are used for this purpose for deriving the proposed topology as shown in Fig. 3.4. The Form 1-C contactors have three contacts: CM (common contact), NC (normally closed contact) and NO (normally open contact) as shown in Fig. 3.4. When the electromagnetic coil is un-energized, the CM contact is connected to the NC, while the NO is kept opened. Energizing the coil toggles the connection of CM from NC to NO.

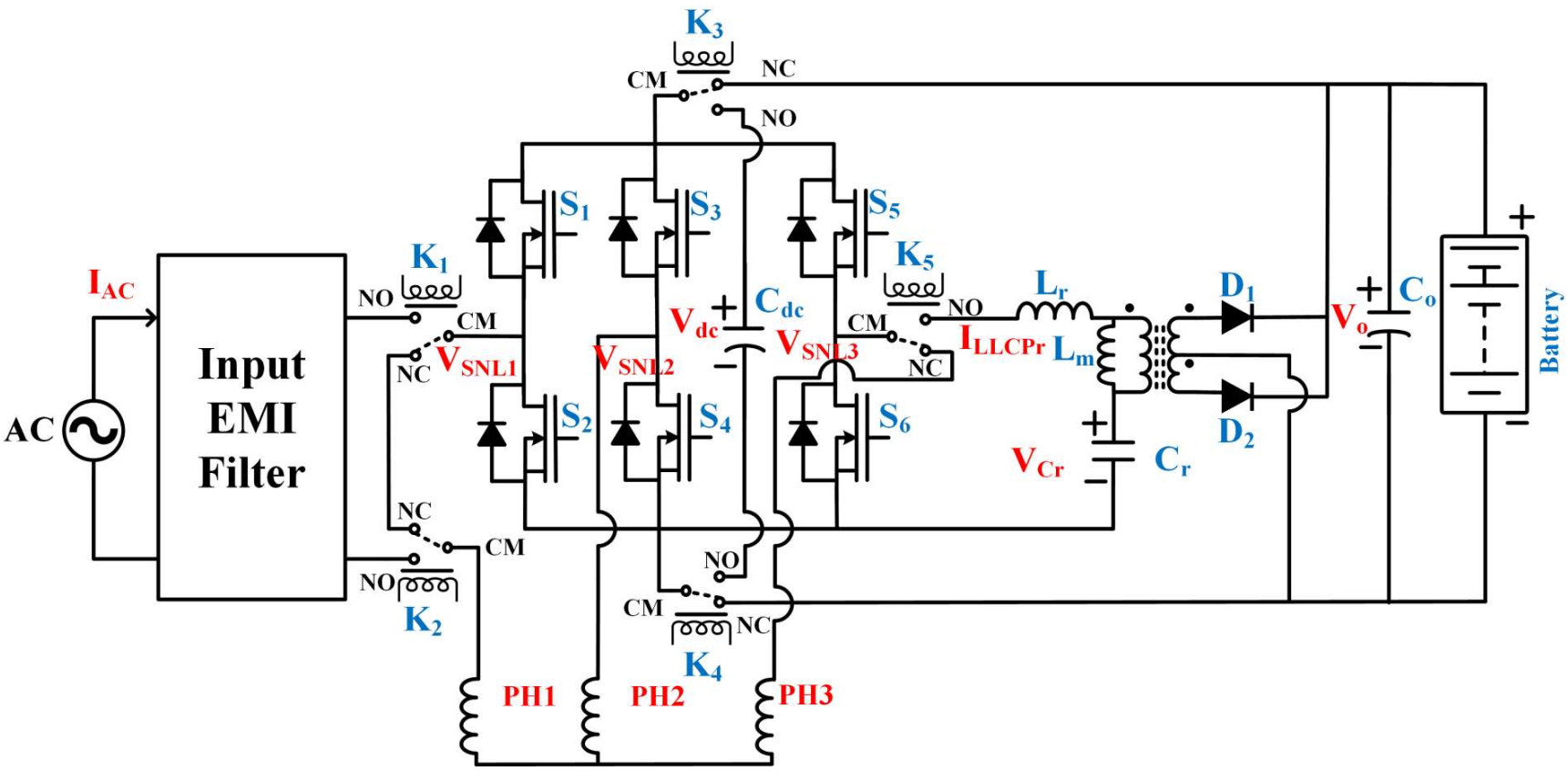

Fig. 3.4. Final reconfigurable on-board power converter (R-OPC) topology.

Table 3.1 Comparison of switch count of available literatures with the proposed converter

Literature	*Nature of Supply*	*No. of stages for battery charging*	*Galvanic isolation*	*No. of MOSFETs / IGBTs*	*No. of Diodes*	*Requirement of separate three - phase VSI unit for propulsion (6 additional switches)*	*Total no. of switches*
[64]	3-phase AC	1	No	12	6	No	18
[65]	1-phase AC	2	No	6	4	No	10
[121]	1-phase AC	2	Yes	6	10	Yes	22
[122]	1-phase AC	1	No	6	4	No	10
[123]	3-phase AC	2	No	9	12	No	21
Proposed	1-phase AC	2	Yes	6	2	No	8

The reconfiguration topology effectively reduces the number of switches as the need of a separate VSI for propulsion unit is eliminated. Table 3.1 compares the switch count of various EV battery charger topologies discussed in chapter 1 with the proposed topology.

3.3 Modes of Operation

3.3.1 Propulsion Mode

The circuit configuration in the propulsion mode is shown in Fig. 3.5. In this mode, the fixed contacts of all the contactors are connected to their respective NC positions. Contactors

K_1 and K_2 isolate the system from the grid and also connect the motor phase PH_1 winding to leg L_A. Similarly, contactors K_3 and K_4 isolate the DC-link capacitor and connect the three -phase inverter bridge to the battery pack. The contactor K_5 isolate the LLC resonant network and closes the motor phase winding PH_3 with leg L_C to complete the three-phase VSI. The diodes D_1 and D_2 are reverse biased and thus prevent the current to flow through the secondary of the transformer and hence eliminate the requirement of additional contactors.

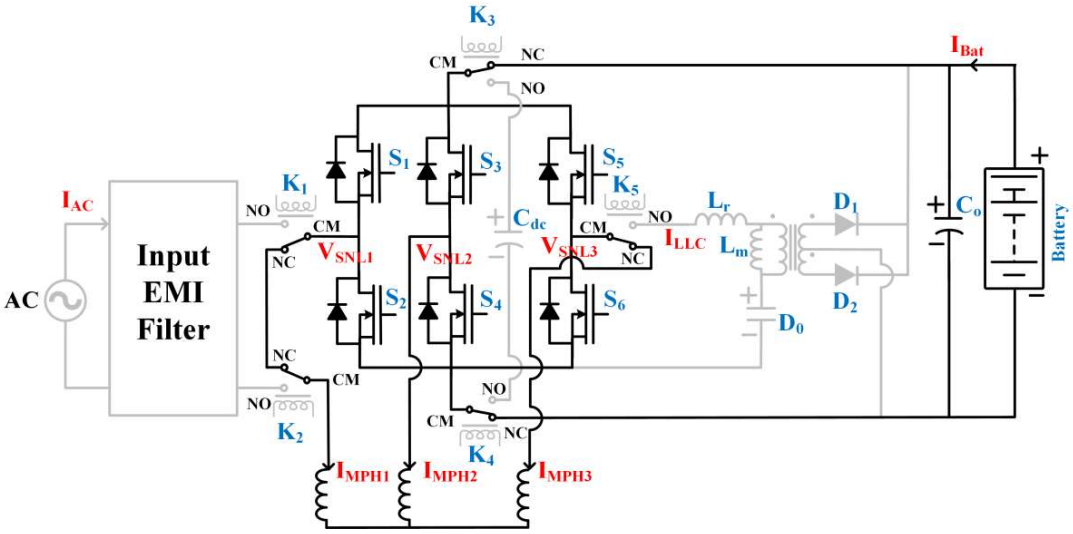

Fig. 3.5. Circuit configuration in propulsion mode.

3.3.2 Charging Mode

In the charging mode, all the contactors are energised to connect their common contacts with corresponding NO positions as shown in Fig. 3.6. The contactor K_1 connects one lead of the grid supply to leg L_A of the charger. The contactor K_2 connects the other lead of grid to the leg L_B of the three -phase inverter bridge through PH_1 and PH_2 motor windings. The contactor K_3 and K_4 isolate the battery pack and connect the DC-link capacitor to the three -phase inverter bridge. The contactor K_5 isolates the motor winding PH_3 of the motor and connects it to the LLC resonant circuit as shown in Fig. 3.6.

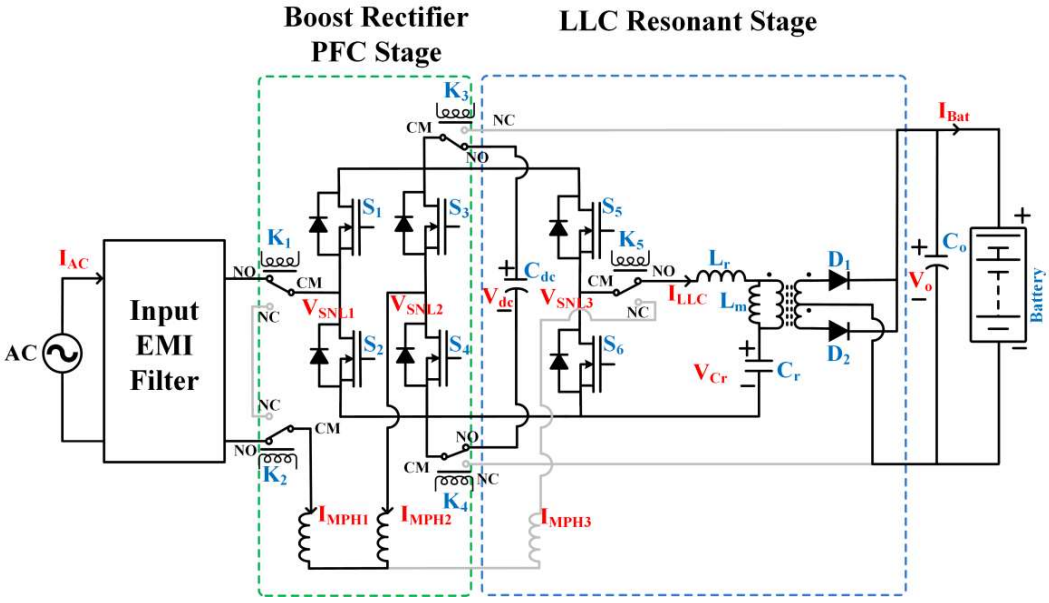

Fig. 3.6. Circuit configuration in charging mode.

Motor phase windings PH_1 and PH_2 are in series and work as the boost inductor at the input side. The switches S_5 and S_6 are used to realize the half-bridge LLC resonant stage. The diodes D_1 and D_2 at the secondary side are used to rectify the secondary side voltage. The battery is charged optimally using the CC-CV charging method.

Switches S_2 and S_4 are switched during the positive and negative half-cycles of the supply voltage respectively. Among the four switches, S_2 and S_4 are operated as the switching of the lower side switches is more convenient. In the positive half-cycle of supply voltage, body diodes of switches S_1 and S_4 are forward biased and switch S_2 is operated according to the PWM control scheme. Similarly, during the negative half-cycle, body diodes of the switches S_2 and S_3 are forward biased and the switch S_4 is switched according to the PWM control scheme.

The operation of AC-DC rectifier as a boost PFC converter during the charging mode is explained by four sub-modes. During submode-1, current flows through switch S_2 and the body diode of switch S_4 to charge the boost inductor in the positive half-cycle of supply voltage as shown in Fig. 3.7 (a). In submode-2, the inductor energy is supplied to the DC-link through the body diodes of S_1 and S_4 to complete the boost operation as shown in Fig. 7(b). Similarly, submode-3 and submode-4 are shown in Fig. 7(c) and Fig. 7(d) respectively for the negative half-cycle of the supply voltage.

The DC-DC converter stage uses a half-bridge LLC resonant converter cascaded with a centre-tapped full-wave rectifier. This stage serves the purpose of galvanic isolation as well as stepping down the DC-link voltage.

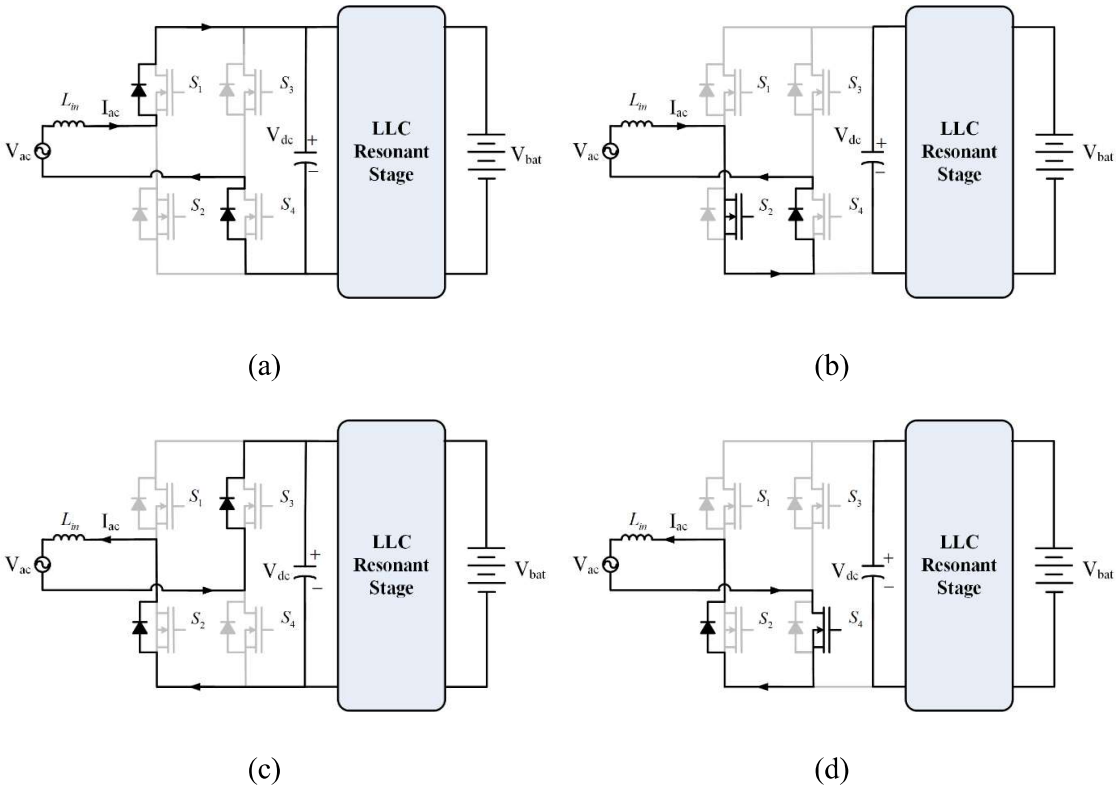

Fig. 3.7. Modes of operation of boost PFC stage: during positive half-cycle (a) S_2 is ON (submode-1) (b) S_2 is OFF (submode-2) and during negative half-cycle: (c) S_4 is ON (submode-3) (d) S_4 is OFF (submode-4).

3.4 Control and Design Analysis

3.4.1 Control Scheme for Propulsion Model

A conventional propulsion model is used to drive the BLDC motor during propulsion mode. The BLDC motor used in this prototype has three in-built binary hall effect sensors, which are positioned symmetrically at 120° among them. Such an arrangement results in a 60° resolution measurement. Thus, the entire cycle of 360° is divided into six equal sectors of 60°. The sensor outputs are used to sense the position of the permanent magnet (PM) flux density wave. Consequently, the switching states are determined according to Table 3.2.

Table 3.2. Switching states of VSI based on hall effect sensors output

Sectors	Position of PM magnetic axis	Outputs of Hall effect Sensors			Switching States					
		H_1	H_2	H_3	S_1	S_2	S_3	S_4	S_5	S_6
I	$330° < \theta \leq 30°$	1	0	0	OFF	OFF	ON	OFF	OFF	ON
II	$30° < \theta \leq 90°$	1	1	0	OFF	ON	ON	OFF	OFF	OFF
III	$90° < \theta \leq 150°$	0	1	0	OFF	ON	OFF	OFF	ON	OFF
IV	$150° < \theta \leq 210°$	0	1	1	OFF	OFF	OFF	ON	ON	OFF
V	$210° < \theta \leq 270°$	0	0	1	ON	OFF	OFF	ON	OFF	OFF
VI	$270° < \theta \leq 330°$	1	0	1	ON	OFF	OFF	OFF	OFF	ON

3.4.2 Control Scheme for Charging Mode

The topology is reconfigured as per Fig. 3.6 during the charging mode. The first stage serves the purpose of an AC/DC boost rectifier, which additionally takes care of the input power factor correction. The objectives of the second stage are to provide galvanic isolation during charging from the grid, ensure soft switching to minimize switching losses and step-down the DC-link voltage for low voltage battery pack. Considering these factors, the LLC resonant converter is chosen as the second stage of the charger.

The modeling and analysis of the half-bridge LLC resonant converter is explained in chapter-1 of the thesis. However, in order to provide the readers a smooth sail, the analysis and design of the half-bridge converter topology is briefed in this subsection also.

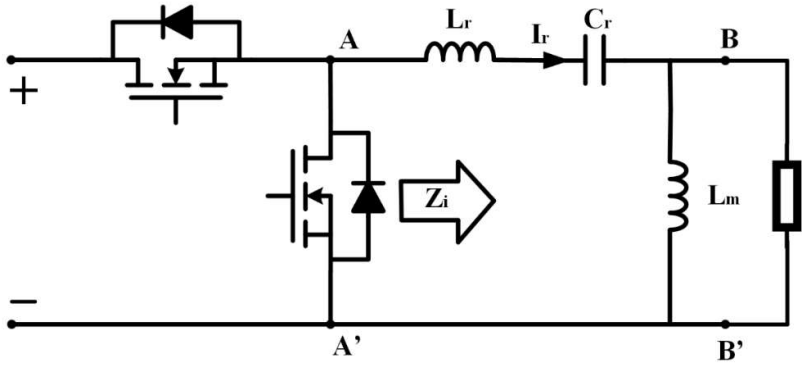

Fig. 3.8. Half-bridge LLC resonant converter.

The half-bridge converter topology is shown in Fig. 3.8. In order to ensure ZVS of the switches, the switch current must lag the voltage across the switches. Hence, the input impedance of the LLC network (Z_i) as seen by the terminals AA' must be inductive in nature [111]. The input impedance (Z_i) as seen by the terminals AA' with resistance R connected across BB' can be expressed as

$$Z_i = \frac{s^3 L_m L_r C_r + s^2 (L_m + L_r) C_r R_{ac} + s L_m + R}{s^2 L_m C_r + s C_r R} \tag{3.1}$$

where

L_r is the series inductance,

L_m is the parallel inductance,

C_r is the resonant capacitance,

R is the resistance across terminals BB'.

The bode diagrams of Z_i for varying load conditions are shown in Fig. 3.9. It is observed from Fig. 3.9 that f_{sc} is the resonant frequency when BB' is short circuited and f_{oc} is the resonant frequency when BB' is open circuited. From the bode diagram, it may be observed that the poles are dominant at frequencies lower than f_{oc} and zeroes are dominant at frequencies higher than f_{sc}. Hence, it can be implied that the input impedance is inductive in nature at frequencies higher than f_{sc} for all load conditions. Therefore, to ensure ZVS, the switching frequency (f_s) of the half-bridge LLC converter must be greater than or equal to f_{sc}.

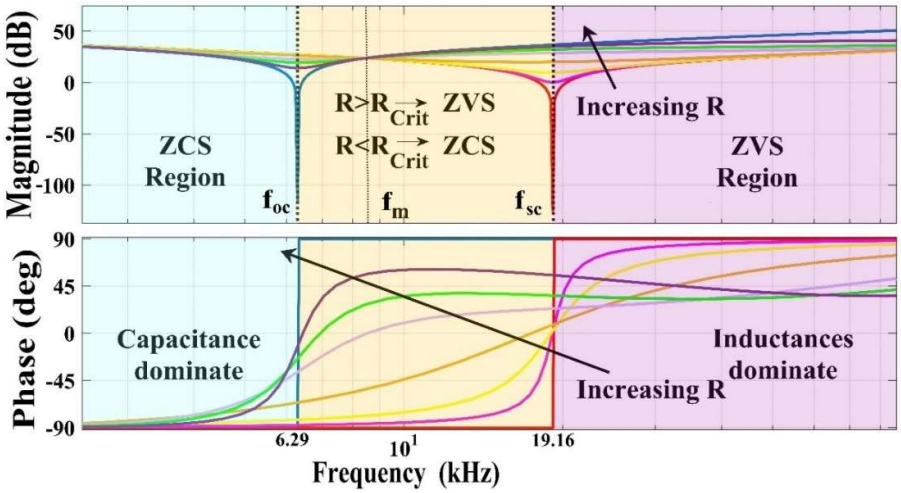

Fig. 3.9. Bode diagrams of Zi for varying load conditions.

The resonant converter also achieves soft switching, which increases the efficiency of the converter. However, the soft switching is ensured through proper designing of the resonant tank elements. Traditional design process of the LLC converter presents several challenges due to the fact that the LLC converters perform power conversion by frequency modulation instead of pulse width modulation and hence require a different design approach. The conventional methods such as steady state averaging method works satisfactorily with pulse width modulation but are not suitable for resonant converters. Different methods have been reported to mathematically model the LLC resonant converter [113], [114]. These methods either do not capture the dynamics over the full range of operation or are mathematically complex. Another frequently used method is to obtain an experimental frequency response plot (experimental bode plot) of the converter for designing the controller [115]. This approach requires a test prototype before the controller is designed. Hence, the first harmonic approximation (FHA) method is widely used for designing the resonant converter. The approximation remains valid in the vicinity of the short circuit resonant frequency (f_{sc}). Through this approximation, the non-linear non-sinusoidal circuit is converted to a linear sinusoidal circuit. The voltage gain of the converter can therefore be expressed as

$$G_{LLC} = \left| \frac{j\omega L_m \parallel R}{(j\omega L_m \parallel R_{ac}) + j\omega L_r + {}^{1}/_{j\omega C_r}} \right| \tag{3.2}$$

Further, the output terminal voltage can be expressed as

$$V_0 = G_{LLC} * \frac{1}{n} * \frac{V_{dc}}{2} \tag{3.3}$$

where n is the transformer turns ratio.

Normalizing the frequency with f_{sc} as base, we can write $f_n = \frac{f_{sw}}{f_{sc}}$. The ratio of the magnetizing inductance to the leakage inductance is expressed as $L_n = \frac{L_m}{L_r}$. The quality factor of the circuit is defined as

$$Q = \frac{1}{\mathrm{R}} \sqrt{\frac{L_r}{C_r}} \tag{3.4}$$

Thus, (3.2) can be rewritten as

$$G_{LLC} = \left| \frac{L_n {f_n}^2}{\{(L_n + 1){f_n}^2 + 1\} + j\{({f_n}^2 - 1) f_n Q_c L_n\}} \right| \tag{3.5}$$

In order to achieve line regulation and load regulation, the converter must be designed for a range of G_{LLC} which contains the maximum and minimum required gain, defined as G_{LLC_min} and G_{LLC_max}. The voltage gain of the LLC resonant converter versus switching frequencies are plotted for different loading conditions (different Q values) and are presented in Fig. 3.10.

As observed from Fig. 3.10, the Q-factor decides the peak gain of the converter. Higher the Q-factor, lower is the peak gain that can be attained. Hence, to achieve peak gain $G_{LLC\_max} > 1$, there must a maximum Q-factor (Q_{max}). If $Q > Q_{max}$, the maximum gain of the converter is less than G_{LLC_max}, which results in unfulfillment of design requirements. Generally, at high power ratings, the load is high which implies that R is very low. From (9), it can be inferred that at high load conditions, the Q-factor tends to be high. This imposes limitations on the gain of the converter. Hence, as a counter measure, L_r must be reduced. It is thus evident that resonant converters demand low leakage inductance at higher power ratings. However, this observation is valid for converters operating under frequency modulation to achieve the required load regulation.

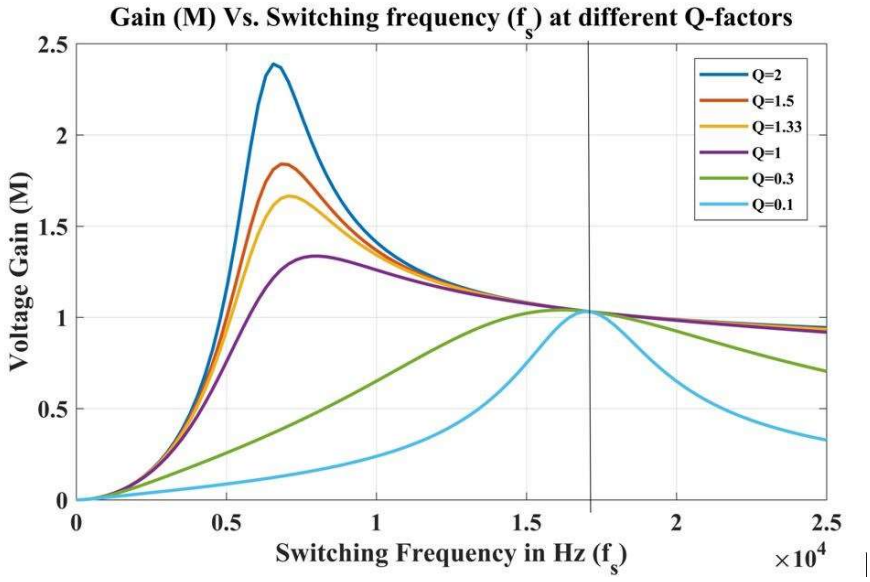

Fig. 3.10. Gain versus frequency curve of half-bridge LLC resonant converter at different Q-factors.

In the proposed work, the converter is designed to operate at f_{sc}, where it provides unity gain for all Q-factor as observed from Fig. 3.10. The DC-link voltage is regulated to achieve the required load regulation. Consequently, the design of the resonant components is independent of Q-factor and the ratio of magnetizing to leakage inductance, which are generally the constraints in the design process. The switching frequency selected initially is 20 kHz in this case, where the derating factor of the ceramic capacitor is negligible. Subsequently, the transformer is designed for a magnetizing to leakage inductance ratio of around 8. The measured magnetizing and leakage inductances are found to be 571 µH and 69 µH respectively. The switching frequency of the converter must be equal to f_{sc} and is expressed as

$$f_{sc} = \frac{1}{2\pi\sqrt{L_r C_r}} \tag{3.6}$$

The resonant capacitor is thus selected according to the following expression such that f_{sc} is around 20 kHz.

$$C_r = \frac{1}{(2\pi f_{sc})^2 L_r} \tag{3.7}$$

The capacitor is selected from standard values is 1 µF and the corresponding calculated resonant frequency is 19.16 kHz.

It is observed that the gain of the converter at the short circuit resonant frequency remains constant for different Q-factors. Hence, if the resonant network is switched at the short circuit resonant frequency, it behaves as a proportional block. The ZVS for all load conditions is also ensured at f_{sc} as discussed before. It is observed from Fig. 3.4 that galvanic isolation and rectification of the output of LLC network is provided by a full wave rectifier with centre-tapped transformer. This centre-tapped configuration inherently provides a gain of 0.5. Furthermore, the half-bridge configuration of the LLC resonant converter also provides a gain of 0.5. Therefore, the effective gain of the second stage is given by,

$$G_s = \frac{1}{4} n G_{LLC} \tag{3.8}$$

where n is the turns ratio of transformer and G_{LLC} is the gain of LLC resonant network.

The gain of the LLC network (G_{LLC}) at the short circuit resonant frequency is unity as observed in Fig. 3.12. Therefore, the gain of the second stage (DC-DC stage) is given by

$$G_s = \frac{1}{4} n \tag{3.9}$$

It can be implied from (3.9) that the gain of the second stage can be designed by selecting suitable transformer turns ratio. Thereafter, the battery terminal voltage is controlled by varying the DC-link voltage [124].

The voltage error to the PFC voltage loop is obtained by comparing the output of the LLC resonant stage with the output reference instead of sensing the DC-link voltage. A gain term $1/G_{LLC}$ is introduced to compensate the proportional gain term of LLC resonant converter (G_{LLC}).

The output capacitor is selected based on its usage during the charging mode. The value of the capacitor is calculated to minimize the ripple content of the output voltage. The output voltage ripple of a full-wave diode rectifier is given as

$$V_{ripple} = \frac{I_{ripple}}{2 f C_O} \tag{3.10}$$

The value of C_O is found to be 1.739 mF considering an output voltage ripple of 0.3% at a switching frequency of 19.16 kHz. As per best available choice in the laboratory, a 2 mF electrolytic capacitor is chosen for the purpose.

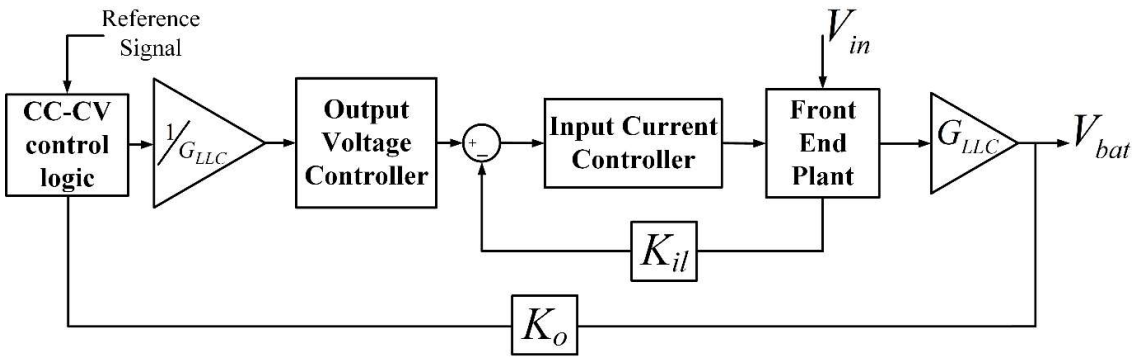

Fig. 3.11. Implementation of unified control scheme for the proposed topology.

It is worth observing that since the second stage acts as a proportional block, it does not require a separate control loop. Hence, the two-stage battery charger can be controlled by a unified control loop as shown in Fig. 3.11. The control loop implements two PI controllers and ensures near-unity power factor operation as well as optimal battery charging. The charging current and battery terminal voltage are also regulated during CC and CV modes of battery charging, respectively. Three standard optimal battery charging techniques are reported in the literature [125]–[127]. They are: CC-CV charging, pulse charging and reflex charging. Among these three charging techniques, the CC-CV charging technique is the most popular one and also widely used in the industry. Therefore, in this paper, the CC-CV charging method is adopted to implement the optimal battery charging of the EV for the developed prototype.

3.5 Experimental Validation

The proposed R-OPC is validated using a 24 V, 400 W BLDC motor and 2x12 V, 30 Ah lead acid batteries. Fig. 3.12 shows the overall implementation of the proposed R-OPC. Hall A, Hall B, and Hall C in Fig. 3.12 indicate the output of three hall effect sensors from the BLDC motor. Considering the size and weight, E-core EE6527 with manganese-zinc ferrite material CF139 is used as the transformer core for the LLC resonant stage. The minimum number of primary turns is taken as 10 for a battery terminal voltage of 48 V and unity turns ratio. The measured values of primary winding leakage inductance (L_r) and the magnetizing inductance (L_m) are 69 μH and 571 μH, respectively. The datasheet for the selected core material shows that the core loss is minimal for switching frequencies less than 20 kHz.

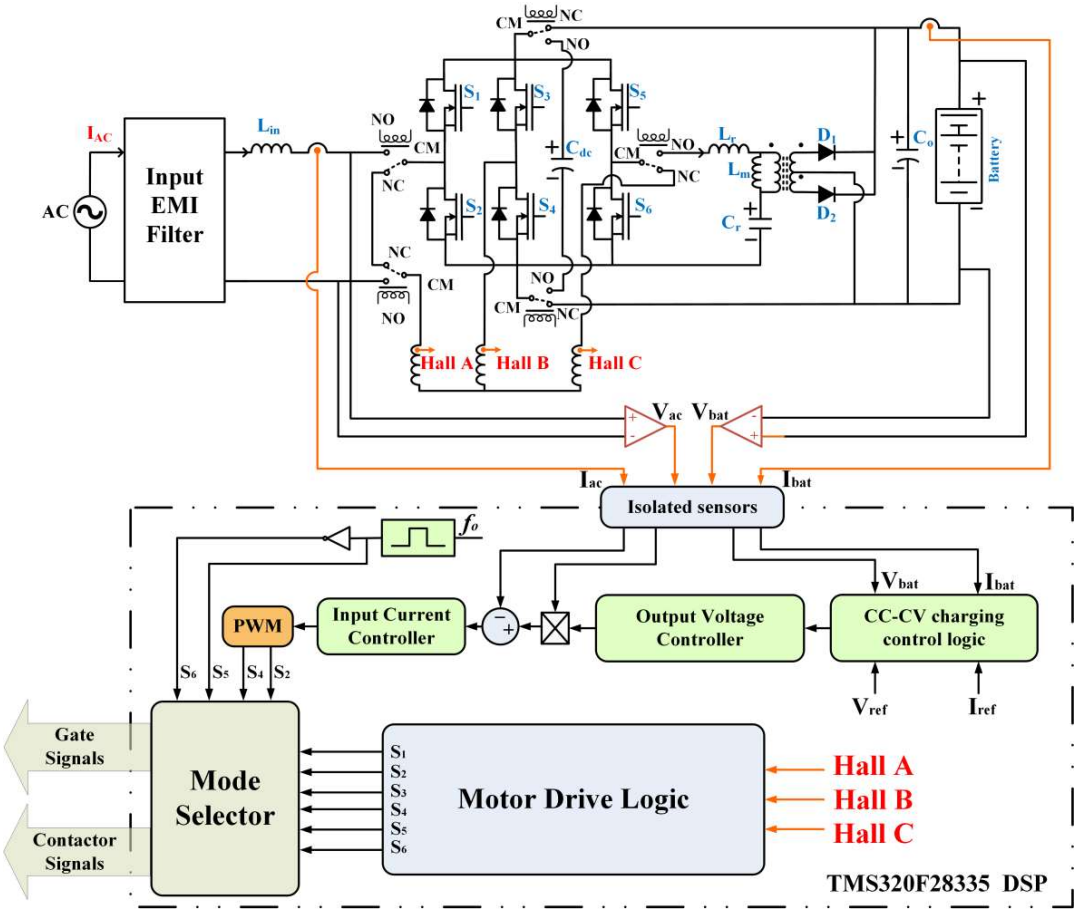

Fig. 3.12. Complete proposed R-OPC with control scheme.

Using (3.10), the resonant capacitance is calculated as 1uF for a switching frequency of 19.16 kHz. A TI TMS320F28335 digital signal processor is used to implement the digital controller. The Fig. 3.13 shows the photograph of the developed prototype for the proposed R-OPC and the components used in the prototype are listed in

Table 3.3. The performance of R-OPC is validated in both charging and propulsion modes. During the charging mode of the proposed R-OPC, the prototype is tested at 470 W for resistive load and to charge a 24 V, 30 Ah lead acid battery using CC-CV charging.

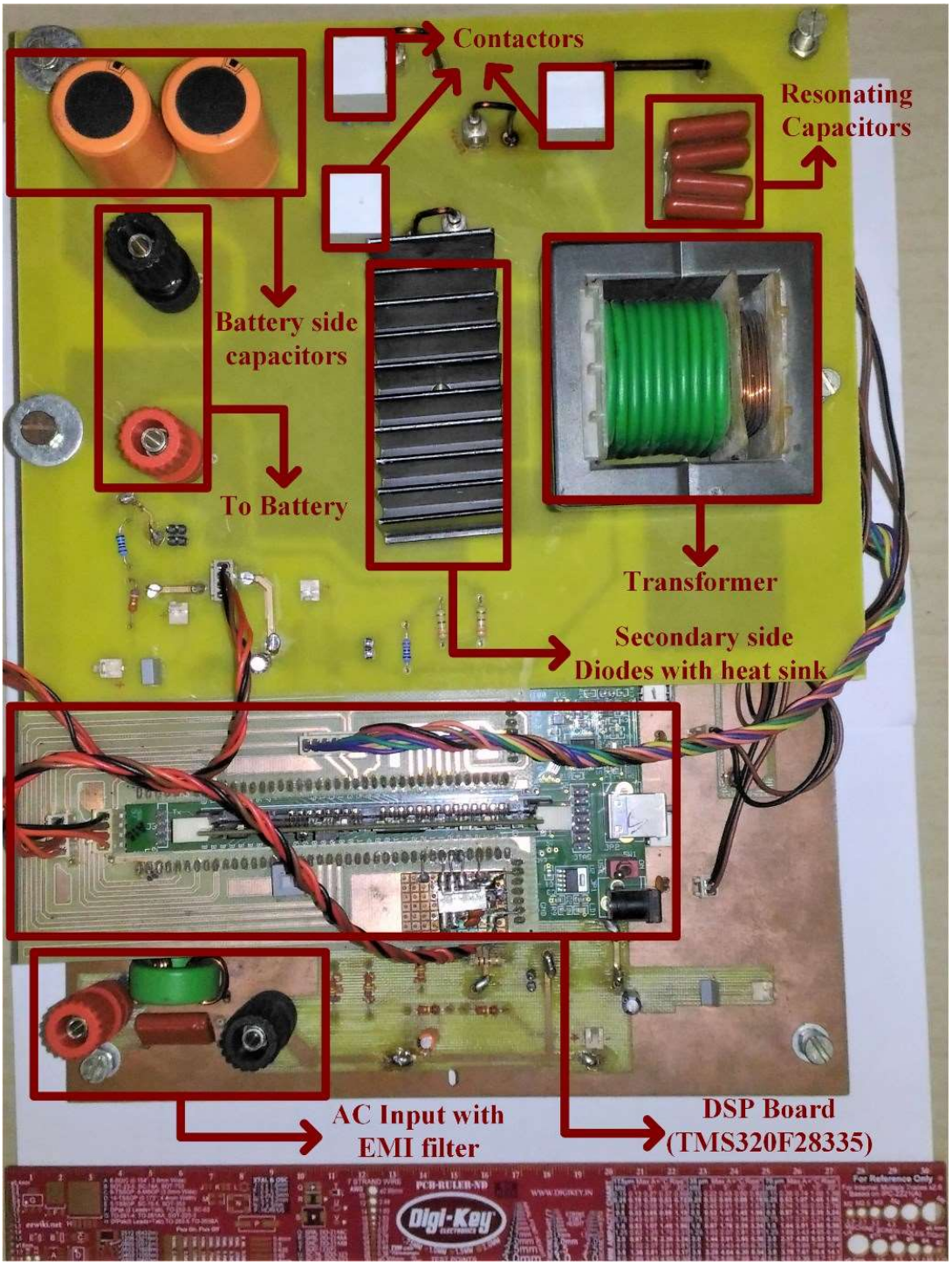

Fig. 3.13. Photograph of the experimental prototype.

Table 3.3. Components Used With Rating

Component	Rating
DC-link Capacitor	1500 µF
Output Capacitor	2000 µF
MOSFET	500 V/20 A
Diode	200 V/20 A
Transformer	L_m = 571 µH, L_r = 69 µH, n = 1
Motor	400 W, three-Phase BLDC
Contactor	400 V, 15 A
Resonant Capacitor	1 µF, 250 V
Batteries	2 x12 V, 30 Ah
Voltage Sensor	320 mV
Current Sensor	20 A

3.5.1 Experimental validation

3.5.1.1 R-OPC during propulsion mode of operation

The operation of R-OPC in propulsion mode is validated through a 400 W, 24 V BLDC motor driven by a 24 V battery pack. Fig. 3.13 shows the motor phase voltages during the propulsion mode, where battery voltage V_{bat} = 24 V. It may be observed from Fig. 3.14 that the BLDC motor phase voltages are phase displaced by 120º. Fig. 3.15 depicts the motor phase currents I_{MPH1}, I_{MPH2} and I_{MPH3}. It can be observed that the phase currents are also displaced by 120º. Experimental results shown in Fig. 3.14 and Fig. 3.15 validate the performance of the R-OPC in propulsion mode with 400 W, 24 V BLDC motor.

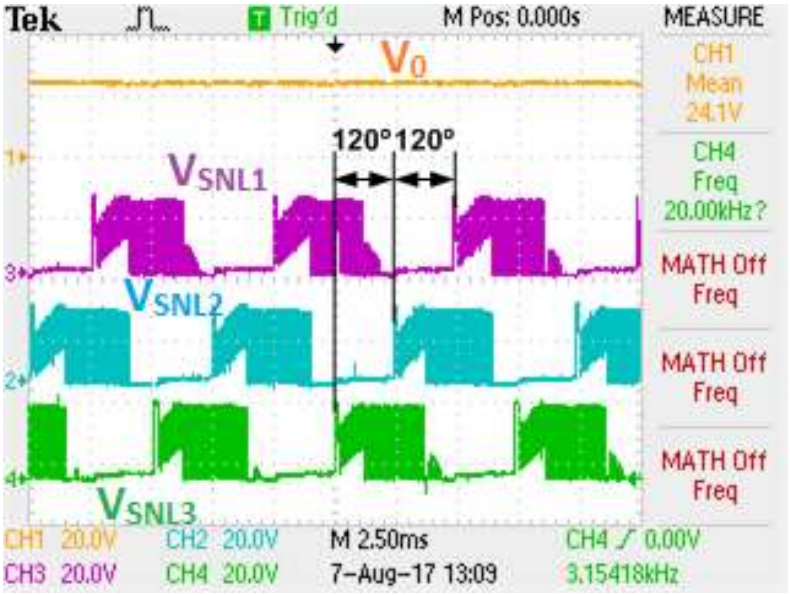

Fig. 3.14.Three phase BLDC motor operation verified by switch node voltages VSNL1(CH3), VSNL2(CH2), VSNL3(CH4) and battery voltage Vbat (CH1) of the R-OPC (at 120^o phase difference) in propulsion mode. (CH1 20 V/ div, CH2 20 V/div, Ch3 20 V/div, CH4 20 V/div).

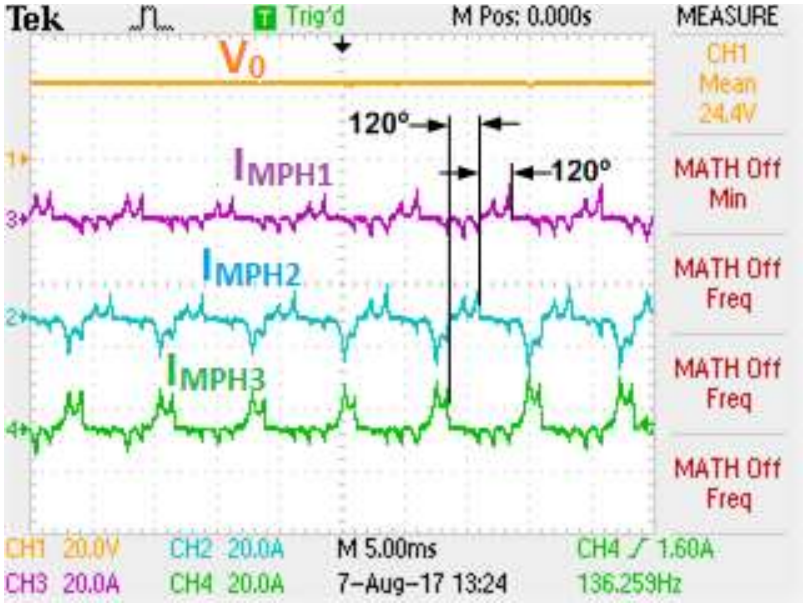

Fig. 3.15. Three -phase operation of BLDC motor verified by motor phase currents IMPH1(CH3), IMPH2(CH2), IMPH3(CH4) and battery terminal voltage Vbat (CH1) of the R-OPC (at 120-degree phase difference) in propulsion mode. (CH1 20 V/ div, CH2 20 A/div, CH3 20 A/div, CH4 20A/div.

3.5.1.2 R-OPC during charging mode of operation

The proposed R-OPC is reconfigured as a two-stage battery charger during charging mode of operation. It is experimentally tested at its rated power of 500 W with resistive load and the captured results are presented in Fig. 3.16. The experiment is performed with a supply AC voltage of 124 V (352 V peak-peak) and source current of 5.9 A (16.8 A peak-peak). The output terminal DC voltage is 48 V with an output current of 9.71 A. Fig. 18 verifies the PFC operation of R-OPC acting as a boost rectifier.

The experimental verification of the LLC resonant stage is shown in Fig. 3.17. This shows that for a DC-link voltage V_{DC} =104 V, current drawn by the LLC stage (I_{LLC}) is 1.64 A (RMS). The half-bridge at the input of the LLC series tank is switching alternatively with a fixed duty ratio of 0.5, which can be observed from Fig. 3.17. The square wave voltage V_{SNL3} varies between 0 V to 104 V, and the voltage across the resonant capacitor V_{cr} =14.85 V (RMS). Fig. 3.17 verifies the ZVS turn-on of the switches of the leg L_C.

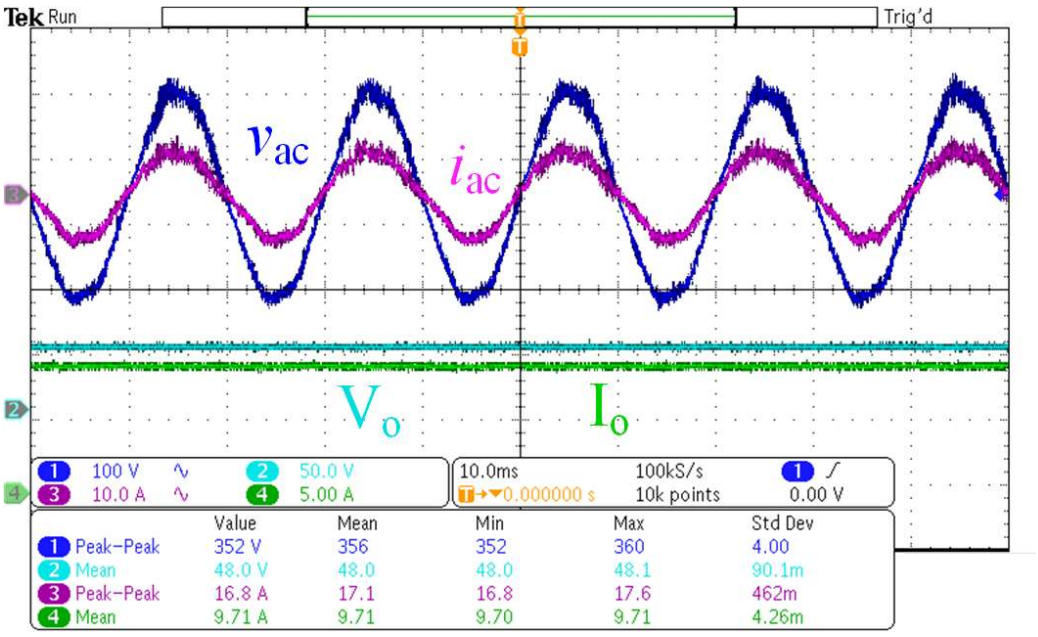

Fig. 3.16. Steady-state waveforms of 470 W prototype: input voltage (V_{ac}) = 352 V (peak-peak), output voltage (V_o) = 48 V, input current (I_{ac}) = 16.8 A (peak-peak), output current (I_o) = 9.71 A.

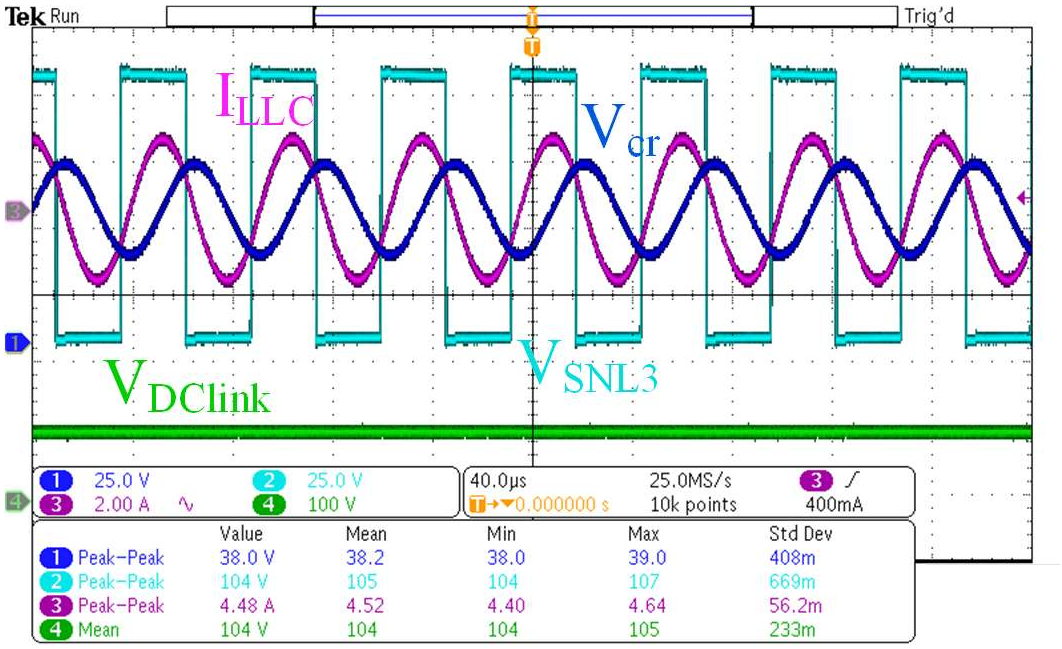

Fig. 3.17. Steady state waveforms of LLC converter: resonant capacitor voltage (V_{cr}) = 42 V (peak-peak), Switch node voltage across S6 (V_{SNL3}) = 104 V (peak-peak), Current through LLC network (I_{LLC}) = 4.64 A(peak-peak), DC-link voltage (V_{dc}) = 104 V.

Fig. 3.18 depicts the motor winding currents along with the supply voltage during the charging mode. In charging mode, motor windings PH_1 and PH_2 are series connected along with an external inductor to increase the boost inductance to a significant value. The currents I_{MPH1} and I_{MPH2} are in phase opposition, while the current I_{MPH3} during charging mode is zero. The reason behind the phase opposition between the two windings is well justified as both the windings are connected back to back to form a series inductor.

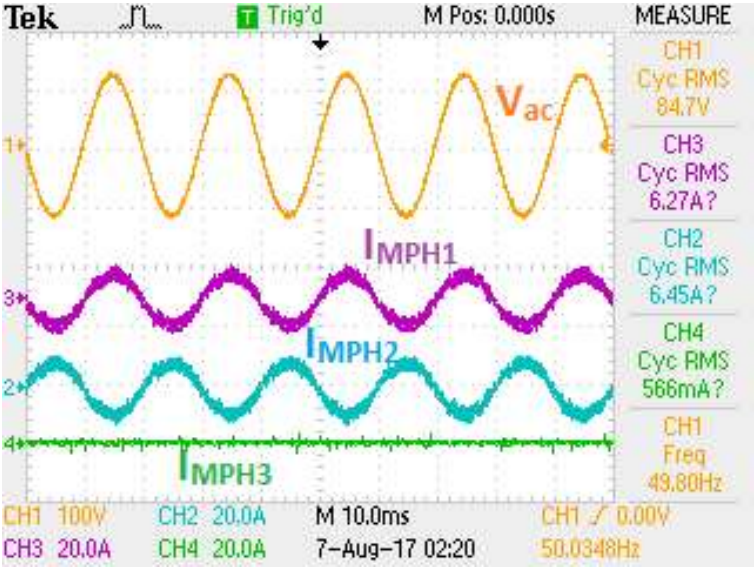

Fig. 3.18. Motor phase 1(CH3), phase 2(CH2) and phase 3(CH4) currents along with input voltage in charging mode. (CH1 50 V/ div, CH2 20A/div, CH3 20A/div CH4 20A/div).

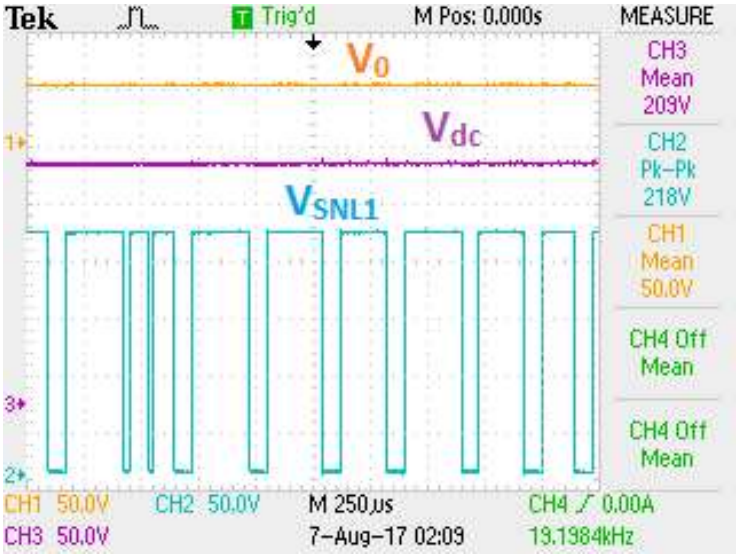

Fig. 3.19. Voltage stress across switch S2 in charging mode at 470 W resistive load. (CH1 50 V/ div, CH2 50 V/div, CH3 50 V/div).

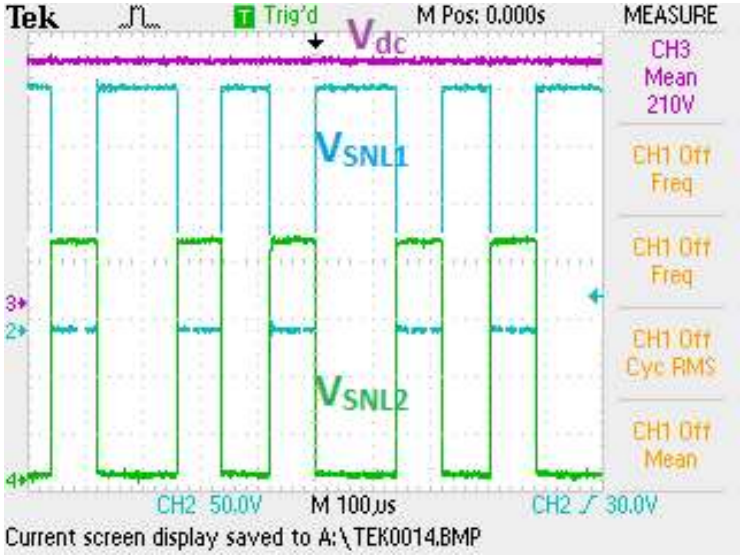

Fig. 3.20. Switch node voltages VSNL1(CH2) and VSNL2(CH4) at 470 W resistive load. (CH2 50 V/div, CH3 50 V/div, CH4 50V/div).

Fig. 3.19 shows the switch node voltage V_{SNL1} along with the DC-link voltage and the output voltage V_0. It is clear from Fig. 3.19 that the switching node voltage V_{SNL1} varies between the common terminal and DC-link voltage, where V_{DC}=209 V and V_0=50 V. Similarly, the voltage stresses across the switches S_2 and S_3 (V_{SNL1} and V_{SNL2}) are shown in Fig. 3.20 for 209 V DC-link voltage. The experimental results shown in Fig. 3.16-Fig. 3.20 confirm the operation of the R-OPC in charging mode for a 470 W prototype.

The proposed R-OPC is tested for dynamic load conditions as a battery is considered to be a variable resistance load during its charging process. The load resistance is subjected to an abrupt change from 10Ω to 5Ω to check the stability of the developed prototype as well as the response time. The captured results during load dynamics is shown in Fig. 3.21. From Fig. 3.21, it can be clearly observed that the load transition results a change in current from 4.855 A to 9.71 A, when the input AC voltage and current are 123 V (RMS) and 3.54 A (RMS), respectively. The result exhibits satisfactory performance in terms of near-unity power factor operation and smooth transition during sudden change in load.

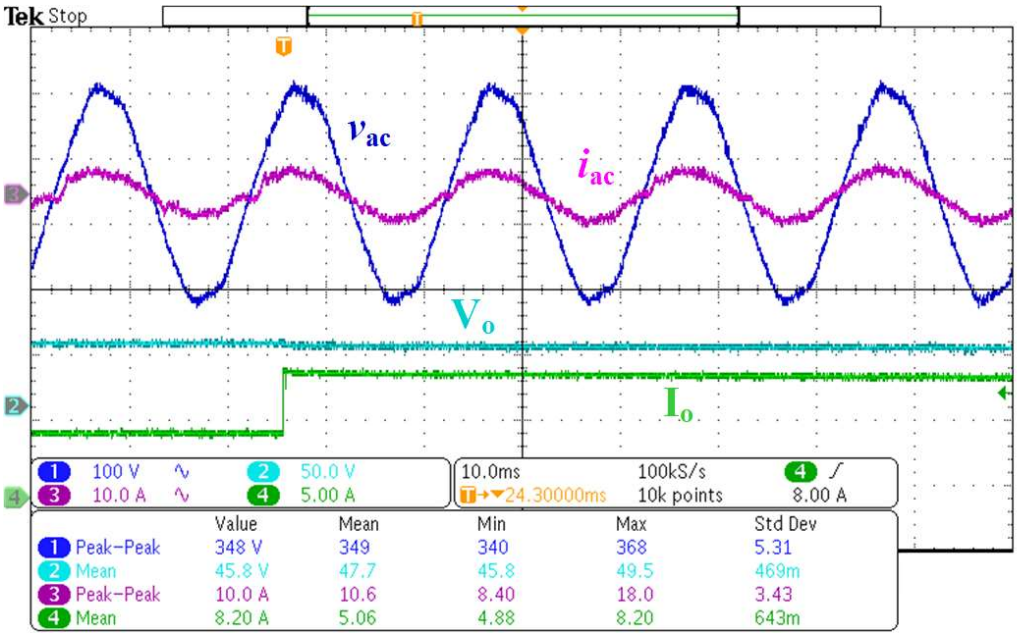

Fig. 3.21. Dynamic response during charging for 50% increase in load current.

3.5.1.3 Optimal charging of 24 V-30 Ah lead acid battery with R-OPC

The CC-CV charging of a 24 V-30 Ah lead acid battery is performed using the laboratory-developed prototype of the proposed R-OPC. The input voltage and current along with the battery terminal voltage and current are captured and are shown in Fig. 3.22. It is evident from Fig. 3.22 that the source voltage V_{ac} and current I_{ac} are in phase, resulting in unity power factor operation during battery charging. Further, it may also be noticed from Fig. 3.22 that the output current I_0 is regulated at 5.52 A. Fig. 3.23 shows the experimentally obtained charging profile of 24 V - 30 Ah lead acid battery. The battery is charged with constant current (CC) for low battery state of charge (SoC) and as soon as the battery voltage reaches 28.7 V, it is charged with constant voltage (CV). The proposed R-OPC also facilitates smooth transition from CC to CV. The results of Fig. 3.22 and Fig. 3.23 confirm the performance of the R-OPC for optimal CC-CV charging of a battery. During the battery charging, the load at the output terminal varies gradually according to the SoC of the battery. The input power factor of the converter and the total harmonic distortion (THD) of current drawn from the supply changes accordingly. While charging the battery, the power factor varies from 0.99 at the beginning to 0.96 at the end of the charging process. Similarly, the THD of input current is found to be 13.8% at the beginning and 23.2 % at the end of the charging process.

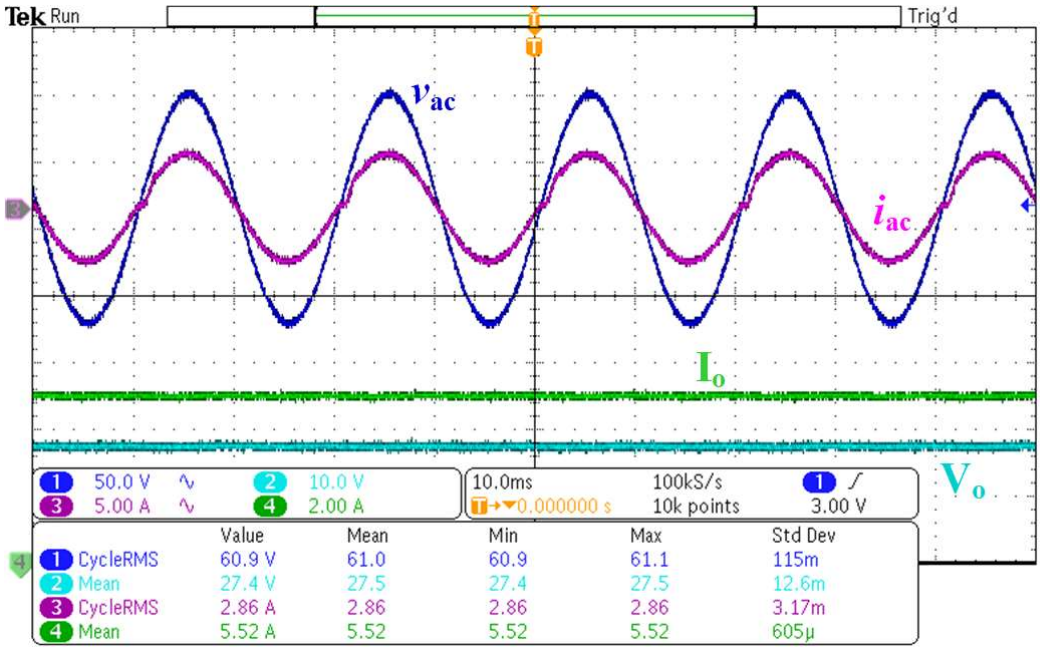

Fig. 3.22. R-OPC operation during charging of 24 V, 30 Ah lead acid battery. Depicted waveforms of source voltage (CH1), battery terminal voltage (CH2), source current (CH3) and charging current (CH4).

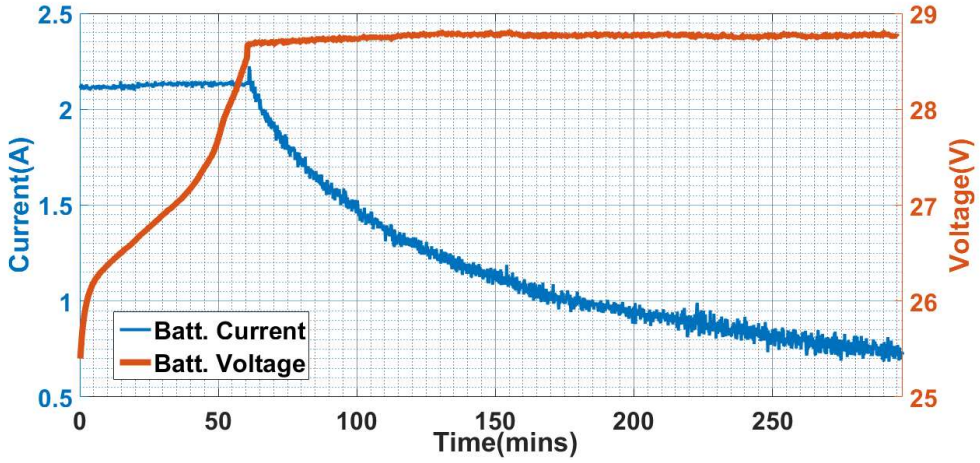

Fig. 3.23. Obtained V-I curve from CC-CV charging of 24 V, 30 Ah lead acid battery with R-OPC.

3.5.2 Impact of Reconfiguration

The objective of reconfiguration is to increase the power density by reducing the number of power electronic components without significantly affecting the efficiency. The proposed reconfigurable topology achieves this by reutilizing the three -phase VSI in the charging mode.

i) Component Utilization Factor

The component utilization factor (CUF) for multimode operation can be expressed separately for the different modes, since the precise duration of each mode is not specified. The CUF, as defined in [128], is the ratio of minimum number of components required for operation with respect to the actual number of components.

$$\text{CUF}=\frac{Minimum\ number\ of\ required\ components}{Actual\ number\ of\ components} \tag{3.11}$$

The CUF of the proposed converter as well as the on-board battery charger topologies available in literature are calculated on the basis of (3.11). Henceforth, they are compared in Table 3.4.

Table 3.4. Comparison of Component Utilization Factor of proposed topology with existing literature

Sl. No.	Literature	Total number of switches (n)	Switches used during charging mode (c)	Switches used during propulsion mode (p)	Charging CUF (c/n)	Propulsion CUF (p/n)
1	[65]	10	10	6	1	0.6
2	[64]	18	18	6	1	0.333
3	[121]	22	16	6	0.7272	0.2727
4	[122]	10	10	6	1	0.6
5	[123]	21	21	6	1	0.2857
6	Proposed	8	8	6	1	0.75

It is observed from Table 3.4 that the CUF in charging mode is unity in all except for [121]. However, the CUF in propulsion mode is considerably improved in the proposed topology. Further, the duration of charging is generally less than the duration of propulsion mode. Therefore, it can be inferred that the overall CUF has been improved.

ii) Power Density Analysis

In case of an on-board charger, it is necessary to carry out the power density analysis as the volume of the power processor plays an important role. The power density can be improved by optimizing certain circuit design parameters [129]. The approach of reconfiguration proposed in this work achieves the same goal on a significant scale. The topology integrates the battery charger and the propulsion unit into a single converter eliminating the requirement of a separate three -phase VSI. A scaled-down laboratory prototype is developed as shown in Fig. 15. The volume of the experimental prototype for the proposed topology is measured to be 9.177 dm^3.The power density for proposed topology rated at 470 W is measured as 51.2 KW/m^3.

i) Efficiency Analysis

The measured efficiency of the proposed prototype at different input AC voltages over the complete range of battery terminal voltage during charging of a 24 V battery pack is presented in Fig. 3.24. It can be inferred from Fig. 3.24 that the efficiency improves with increasing input AC voltage. However, the input voltage magnitude is limited by the rating of the experimental setup. The peak efficiency achieved is 97.6% during charging at an input AC voltage of 70 V.

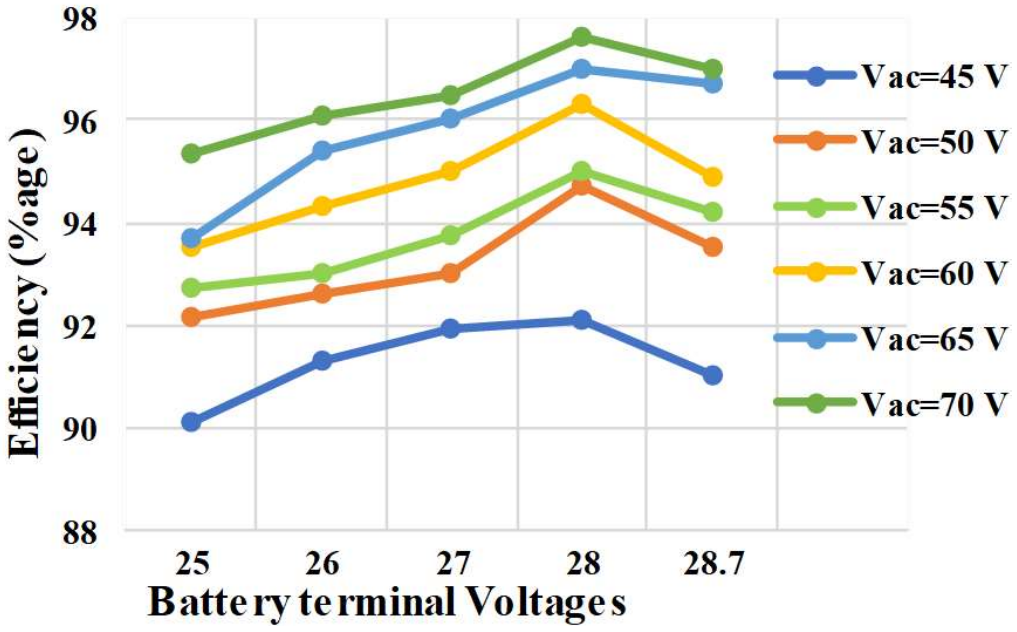

Fig. 3.24. Efficiency curves for different input voltages.

3.6 Conclusion

A reconfigurable on-board power converter (R-OPC) for EVs is presented in this chapter. A three -phase, 6-switch VSI is reconfigured to serve both charging and propulsion of the EV, thus improving the overall power density of the on-board charger. The detailed operation of the proposed R-OPC in both charging and propulsion modes are presented in the chapter. The motor phase windings are reutilized as circuit inductances during charging mode, which further improves the power density of the topology. The mode transition is achieved with the help of switching of contactors. The contactors are operated in zero current condition eliminating switching losses across the contactors during mode transition. The proposed approach achieves improvement in power density and reduction in switch-count as compared to recent literatures presenting contemporary power converters for EVs. A unified control loop scheme capable of near unity power factor operation at the input stage and performing optimal CC-CV charging of the battery in one single control loop is also implemented. A 500 W prototype is developed to validate the performance of the proposed R-OPC. The proposed R-OPC is also validated using CC-CV charging of a 24 V, 30 Ah lead acid battery.

Though the presented idea in this chapter is capable to achieve both the propulsion and charging operation using a single power processor, this concept lags in supporting advance and

user-friendly features like wireless charging option. Wireless EV charging allows the users to charge their vehicle without connecting physical wires, which is safer as compared to wired charging options and it offers convenience to the EV users. In order to include such advance facility like wireless charging, a novel power processor is proposed in the next chapter that offers the user to set-up wireless charging system in home garage, tapping power from a single-phase AC power supply.